Mechanical pressure-mediated Pd active sites formation in NaY zeolite catalysts for indirect oxidative carbonylation of methanol to dimethyl carbonate

Chunzheng Wang, Ningkun Xu, Ting-Ting Liu, Weisong Xu, Hailing Guo, Yanpeng Li, Peng Bai, Xin-Ping Wu, Xue-Qing Gong, Xinmei Liu, et al.

Mechanical pressure-mediated Pd active sites formation in NaY zeolite catalysts for indirect oxidative carbonylation of methanol to dimethyl carbonate

Chunzheng Wang,[a] Ningkun Xu,[a] Ting-Ting Liu,[b] Weisong Xu,[a] Hailing Guo,[a] Yanpeng Li,[a] Peng Bai,[a] Xin-Ping Wu,[b,*] Xue-Qing Gong,[b] Xinmei Liu,[a,*] Svetlana Mintova[a,c,*]

[a] *State Key Laboratory of Heavy Oil Processing, College of Chemical Engineering, China University of Petroleum (East China), Qingdao 266580, Shandong, China*

[b] *Key Laboratory for Advanced Materials and Joint International Research Laboratory for Precision Chemistry and Molecular Engineering, Feringa Nobel Prize Scientist Joint Research Center, Centre for Computational Chemistry and Research Institute of Industrial Catalysis, School of Chemistry and Molecular Engineering, East China University of Science and Technology, Shanghai, 200237, China*

[c] *Laboratoire Catalyse et Spectrochimie (LCS), Normandie Université, ENSICAEN, UNICAEN, CNRS, 6 boulevard Maréchal Juin, Caen 14050, France*

[*] Corresponding authors. E-mail addresses: xpwu@ecust.edu.cn (X.-P. Wu), lxmei@upc.edu.cn (X. Liu), svetlana.mintova@ensicaen.fr (S. Mintova)

Abstract

The structural transformation of metal-containing zeolite catalysts subjected to mechanical compression is often disregarded in the preparation of catalysts. Herein, the impact of the mechanical compression on the catalytic active sites of Pd/NaY catalysts responsible for the indirect oxidative carbonylation of methanol to dimethyl carbonate (DMC) has been disclosed. The DMC selectivity of the catalysts was found to strongly depend on the mechanical-pressure applied, as the mechanical pressure controlled the ratio of $Pd^{(2+\delta)+}$ and $Pd^{\delta+}$ species ($0 < \delta \leq 2$) in the catalysts. The mono-dispersed Pd clusters (1.3 nm) in the Pd/NaY catalyst were obtained under mechanical treatment of 300 MPa. This catalyst showed high CO conversion of 89% and DMC selectivity of 83%, that maintained for at least 150 h. Combining experimental and density functional theory studies, we revealed that the $Pd^{\delta+}$ rather than the $Pd^{(2+\delta)+}$ species enhanced the adsorption of CO and CH_3ONO reactants and inhibited the decomposition of CH_3ONO reactant into byproducts, and thus enhanced the DMC selectivity. The mechanical pressure applied had a noticeable effect on the structural features of the metal-containing zeolite catalysts, but despite its importance, this aspect has been poorly considered in the field of heterogenous catalysis.

Keywords: Mechanical pressure; Active site; Palladium; NaY; Carbonylation; Dimethyl carbonate

1. Introduction

In commercial applications, heterogenous catalysts are seldom utilized in a powder form, and thus the catalyst shaping is indispensable to be implemented in industrial reactors [1–3]. Several shaping methods are used, among which the most important are extrusion, spray drying, tableting and granulation [4,5]. Among these methods, the tableting method produces the most regularly shaped bodies such as pellets and cylinders, which often have high mechanical strength [6,7]. However, the tableting process is often conducted by trial-and-error approach [8]. The tableting method is often proprietary, and the related patents provided a range of shaping conditions and rarely disclosed any details [9,10]. In most cases, there is a huge difference in the performance of catalysts in powder and the shaped forms [11]. Therefore, understanding the chemical and structural features of catalysts behind tableting process is desirable for both fundamental research and commercial applications.

High-pressure inorganic chemistry is one of the “Top Ten Emerging Technologies in Chemistry 2020” reported by the International Union of Pure and Applied Chemistry (IUPAC). Previous high-pressure studies of zeolites revealed unusual structural and chemical changes [12–14]. Several zeolites were amorphized under high pressure, i.e., pressure-induced full or partial amorphization reverting back to the original crystalline structure upon decompression [15,16]. The partly disordered structure resulted from the local collapse and distortion of zeolite framework, which

was closely related to the properties of charge-balancing cations in the zeolites [17]. Lee et al. reported that high pressure of 1.9 GPa led to the irreversible migration and rearrangement of charge-balancing cations, i.e., pressure-induced migration, and to the formation of super-hydrated zeolite with a doubled water content described as pressure-induced hydration [18]. They also suggested that the structural changes of zeolites under high pressure were mediated by the charge-balancing cations and their coordination environment, which could drive the changes in the order-disorder/disorder-order transitions and framework distortion [19]. Jordá et al. demonstrated that ITQ-29 zeolite with LTA topology was transformed into a new ITQ-50 zeolite under a high pressure of 3.2 GPa [20]. The behavior of metal-containing zeolite catalysts under high pressure has not been systematically investigated. It is worthwhile to study whether the catalytic performance of metal-containing zeolite catalysts is dependent on the mechanical pressure, and if so, to what extent.

Green and sustainable manufacture of valuable commercial chemicals based on C1 chemistry via one-carbon feedstocks from abundant carbon resources such as shale gas and coal, is an emerging alternative to the petroleum routes [21–23]. Dimethyl carbonate (DMC) is a green, versatile compound which can be used as a methylating and methoxycarbonylating agent, fuel additive, electrolyte liquid carrier for lithium-ion batteries, as well as for polycarbonate and isocyanate syntheses [24,25]. The traditional production of DMC ($(CH_3O)_2CO$) involves the utilization of a

toxic feedstock, phosgene ($COCl_2$) [26]. In the past decade, extensive studies have been carried out to develop environmentally sustainable and efficient processes for DMC production including the transesterification of methanol (CH_3OH) with ethylene/propylene carbonate, the direct synthesis from carbon dioxide (CO_2) and CH_3OH, the alcoholysis of urea, and direct/indirect oxidative carbonylation of CH_3OH [27–29]. Among these methods, the indirect oxidative carbonylation of methanol to DMC has gained substantial interest due to the cheap raw materials, mild operation conditions and high atom efficiency [30]. This process involves two separate reactions presented in Scheme S1 in Supporting Information (SI): (1) Pd-catalyzed oxidative carbonylation to DMC: $CO + 2CH_3ONO \rightarrow (CH_3O)_2CO + 2NO$, and (2) non-catalytic methyl nitrite (CH_3ONO) regeneration with recycled NO: $2CH_3OH + 2NO + 1/2O_2 \rightarrow 2CH_3ONO + H_2O$. The overall reaction ($CO + 2CH_3OH + 1/2O_2 \rightarrow (CH_3O)_2CO + H_2O$) is a green and efficient process converting C1 feedstocks (CO and CH_3OH) to C2 product.

The gas-phase indirect oxidative carbonylation of methanol to DMC has been industrially implemented by Ube Industries, Ltd., Japan, using a $PdCl_2$/active-carbon catalyst [31,32]. However, chlorine such as hydrogen chloride (100 $\mu L\ L^{-1}$) must be added into the reactants to prevent the Pd sintering and maintain the activity of chlorine-containing catalyst [32,33]. There is an incentive to eliminate chlorine from this process to reduce costs associated with equipment corrosion, chlorine regeneration and generation, product purification and emissions. Consequently, the

development of chlorine-free, high-performance Pd catalysts is highly desirable for the DMC synthesis. Various chlorine-free Pd catalysts have been investigated, and the most appropriate catalyst support was NaY zeolite in comparison to NaX, γ-Al_2O_3, α-Al_2O_3, silica, and MgO [31,34,35]. Guo et al. revealed that the copper promoter could improve the Pd dispersion and maintain the Pd^{2+} active sites on the Pd/NaY catalyst [36]. Dong et al. reported that potassium-doped Pd/NaY catalyst enhanced the activation of CO reactant by forming a Pd-CO···K^+ structure [37]. They also revealed that Lewis acidity of the Pd/NaY catalyst favored the DMC formation, while Brønsted acidity could accelerate the undesired decomposition of CH_3ONO reactant into methyl formate and dimethoxymethane byproducts [34]. Tan et al. found that the catalytic activity of the Pd/NaY catalyst was related to the high oxidation state of Pd species, which could be tuned by the organic ligands [38]. They also demonstrated, by performing density functional theory (DFT) calculations, that the mononuclear-isolated Pd^{2+} centers are critical for high DMC selectivity while the aggregation of Pd species was responsible for the formation of dimethyl oxalate byproduct [35]. The possible mechanism of the reaction followed oxidative addition and reductive elimination, and consisted of (1) oxidization of Pd^0 species by methyl nitrite (CH_3ONO) reactant to generate NO-Pd^{2+}-OCH_3, (2) insertion of adsorbed CO into NO-Pd^{2+}-OCH_3 to form NO-Pd^{2+}-$COOCH_3$, and (3) the reaction between NO-Pd^{2+}-$COOCH_3$ and NO-Pd^{2+}-OCH_3 to yield DMC [33,39]. The Pd^{2+} species are generally considered to be the active sites for the formation of DMC [30,33,35]. In

view of the redox cycle of active sites, the function of Pd^0 species is still under discussion. Yamamoto et al. reported that Pd/NaY catalyst showed a delayed deactivation and decreased by about 50% after 300 h test [40]. Tan et al. found that Pd/NaY catalyst with mononuclear-isolated Pd^{2+} centers was stable for at least 100 h [35], but the selectivity of inevitable byproducts such as methyl formate and dimethoxymethane was not disclosed. Recently, we reported on the preparation of stable Pd/EMT catalyst tested for 130 h. We found that the EMT zeolite framework could inhibit the palladium sintering and maintain the Pd^{2+} active sites [41]. The chlorine-free Pd-based catalysts are still under development, and the bottleneck for their industrialization is the lack of sufficiently active and stable catalysts.

Herein, we presented the mechanical pressure-mediated preparation of Pd-containing NaY zeolite catalyst (Pd/NaY) by a tableting method. The Pd/NaY catalyst was tested in the reaction of indirect oxidative carbonylation of methanol to DMC. The structural changes that took place during the mechanical compression of the Pd/NaY catalyst and their effects on the catalytic performance in the DMC synthesis were disclosed.

2. Experimental

2.1. Catalyst preparation

NaY zeolite was kindly supplied by Daqing Chemical Research Center, China. Prior to the ion exchange, the NaY zeolite was pre-activated at 550 ºC for 2 h under

static air. In a typical process, 16.7 mg palladium chloride ($PdCl_2$, Sinopharm Chemical Reagent Co., Ltd., China) was dissolved in 1.2 mL, 0.94 mol L^{-1} ammonia (NH_3) solution to form a clear palladium ammonia complex ($Pd(NH_3)_4Cl_2$) solution. The $Pd(NH_3)_4Cl_2$ solution was added dropwise into the activated NaY zeolite slurry containing 1.0 g zeolite and 100.0 g deionized water. The resulting suspension was stirred at room temperature (25 ºC) for 12 h and subsequently was heated at 80 ºC to evaporate the excess ammonia until the pH value of the suspension decreased to 7.0–7.2 [35,36]. Then the solid was collected by vacuum filtration and washed thoroughly with deionized water. After drying at 80 ºC for 6 h, the sample was calcined at 200 ºC for 2 h under static air. The as-prepared Pd/NaY catalyst had a Si/Al molar ratio of 2.8 and a Pd loading of 1.0 wt%, corresponding to roughly 1.2 Pd atoms per unit cell, which was determined by inductively coupled plasma-atomic emission spectroscopy (ICP-AES).

As known, the shaping pressure applied for commercial catalysts is in the range of 100–1000 MPa using the tableting process [9]. To study the effect of the mechanical pressure, the as-prepared Pd/NaY catalyst was subjected to treatment under pressure in the range of 60–600 MPa (Fig. S1). After the mechanical compression, the samples were crushed and sieved into 60–80 mesh. The as-obtained catalysts in pellet form were denoted as Pd/NaY-*x*, where *x* corresponds to the mechanical pressure (an example, the catalyst shaped at 300 MPa was named as Pd/NaY-300).

2.2. Characterizations

Transmission electron microscopy (TEM) images of the catalysts were recorded using a JEOL JEM-2100 TEM instrument. High-angle annular dark-field scanning transmission electron microscopy (HAADF-STEM) images were taken on a JEOL JEM-2100F STEM instrument. The chemical composition of the samples was determined by an energy dispersive X-ray spectrometer (EDS). Scanning electron microscopy (SEM) images were acquired on a JEOL JSM-7900F SEM instrument. The Pd loading and Si/Al molar ratio of the samples were measured by inductively coupled plasma-atomic emission spectroscopy (ICP-AES) on a Thermo IRIS Intrepid II XSP. The X-ray photoelectron spectroscopy (XPS) spectra were recorded on an Escalab 250xi spectrometer with an Al Kα radiation. All binding energies were referenced to the C 1s peak at 284.6 eV. The solid-state ^{29}Si cross-polarization magic-angle spinning nuclear magnetic resonance (CP MAS NMR), and single pulse ^{29}Si MAS NMR spectra were measured on a Bruker Advance 400 spectrometer. The chemical shifts were referenced to the kaolin (–91 ppm).

X-ray diffraction (XRD) patterns of the catalysts were obtained using a Bruker D8 Advance diffractometer with a Cu Kα radiation. The relative crystallinity of the samples was determined by measuring the sum of eight Bragg peak areas, namely (331), (511), (440), (533), (642), (822), (555) and (664), and related to the peaks area of the reference sample [42]. The Pd/NaY powder catalyst before the mechanical compression was taken as a reference assigning 100% of crystallinity. After

subtracting the background and kα2 line broadening from the obtained patterns, the average crystallite sizes were estimated using the Scherrer equation [43].

The unit cell parameter (α) of the samples was determined from the (555) reflection, using pure silicon as an internal standard [42]. The framework Si/Al molar ratio of the samples was estimated from the unit cell parameter (α) by the following equation [42]:

$$\text{Si/Al ratio} = \frac{25.858 - \alpha}{\alpha - 24.191}$$

Textural features of the samples were analyzed by N_2 physisorption isotherms measured at −196 ºC using a Quantachrome Autosorb-IQ3 instrument. The specific surface area was calculated using the Brunauer-Emmett-Teller (BET) method; the pore size distribution was determined by the DFT model from the adsorption branch of the N_2 sorption isotherms.

In situ diffuse reflectance infrared Fourier transform spectroscopy (DRIFTS) experiments with a carbon monoxide (CO) probe molecule were performed in a Harrick Scientific HVC-DRP-4 cell fitted with ZnSe windows using a Bruker Vertex 70 spectrometer, equipped with a mercury-cadmium-telluride (MCT) detector. The sample temperature was monitored by a K-type thermocouple welded onto the top center of the cell. Typically, about 0.002 g sample without diluents was pre-treated in N_2 flow (80 mL min^{-1}) at 200 ºC for 1 h, and then cooled down to 30 ºC for taking a background spectrum. The adsorption of CO was conducted at 30 ºC using a gas mixture of 10 vol% CO in N_2. After that, the sample was purged thoroughly with pure

N_2 and then the DRIFTS spectra were recorded at 30 ºC and 50 ºC. Each spectrum was obtained using the Kubelka-Munk mode from 4000 cm^{-1} to 600 cm^{-1} (4 cm^{-1} resolution and 32 scans).

2.3. Reactivity tests

The schematic diagram of the setup used for the catalytic test is presented in Scheme S2 (Supporting Information, SI). The indirect oxidative carbonylation of methanol to DMC was performed in a continuous-flow-type fixed-bed microreactor (quartz tube, 8 mm i.d.) under 0.1 MPa. Quartz wool was placed below the catalyst bed to hold the catalyst. The reaction temperature was maintained using a tube furnace equipped with a temperature-programed controller and a K-type thermocouple. The reactant of methyl nitrite (CH_3ONO) was prepared though an esterification reaction ($2NaNO_2 + 2CH_3OH + H_2SO_4 \rightarrow 2CH_3ONO \uparrow + Na_2SO_4 + 2H_2O$) in the laboratory. The methyl nitrite gas was collected into a steel cylinder and then mixed with 99.99 vol% N_2 to form a gas mixture of CH_3ONO/N_2 (1/4, mole). The 99.99 vol% N_2, gas mixtures of CO/N_2 (1/9, mole) and CH_3ONO/N_2 (1/4, mole) were fed via three calibrated mass flow meters, respectively. The gas hourly space velocity (GHSV) and reaction temperature were varied in the range of 4000–800000 mL $g_{cat.}^{-1}$ h^{-1} and 100–120 ºC, respectively. Analysis of product stream was conducted using an online gas chromatography (Agilent 7890B). A thermal conductivity detector (TCD, 2.5-m molecular sieve 5A and 1.0-m HayeSep Q packed columns, Agilent) was

used to measure the CO and N_2. A flame ionization detector (FID, 30-m HP-Innowax capillary column, Agilent) was employed to detect the CH_3ONO, DMC, dimethoxymethane and methyl formate. The kinetic experiments, and the calculations of the turnover frequency (TOF), Thiele modulus, effectiveness factor, CH_3ONO conversion, CO conversion, DMC, dimethoxymethane and methyl formate selectivity were presented in SI.

3. Results and discussion

3.1. General properties of Pd/NaY catalysts prepared under treatment with different mechanical pressures

The morphologies of the Pd/NaY catalysts prepared under treatment with different mechanical pressures are presented in Fig. 1. The Pd/NaY-60 catalyst consisted of aggregated crystals with a size of 300–500 nm (Fig. 1a). With increasing the mechanical pressure from 60 MPa to 150 MPa, the mechanical compression led to the fragmentation of several zeolite crystals, and consequently, sporadic small crystals were found on the Pd/NaY-150 catalyst as marked with red circles in Fig. 1b. With further increasing the mechanical pressure, more and more primary zeolite crystals were fragmented into small pieces as observed by SEM (Fig. 1c–e). In line with the SEM, the TEM pictures revealed the gradual decrease of average crystal size from 370 nm to 180 nm with enhancing the mechanical pressure (Table 1). Even though the Scherrer equation is not highly accurate when the crystal size is larger than 100 nm [44], the crystal size estimated based on the XRD study showed a similar trend to the

TEM observation (Table 1).

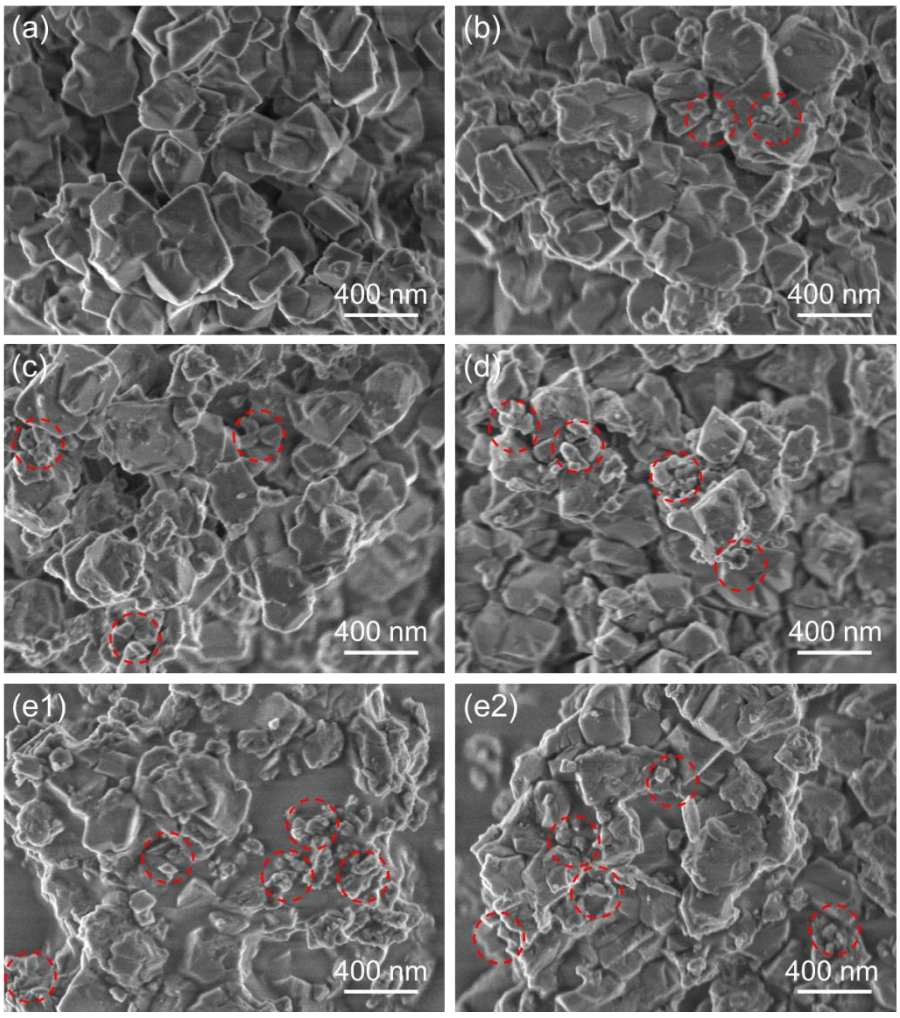

Fig. 1. SEM images of the Pd/NaY catalysts prepared under treatment with different mechanical pressures: (a) Pd/NaY-60, (b) Pd/NaY-150, (c) Pd/NaY-300, (d) Pd/NaY-450 and (e1,e2) Pd/NaY-600. The fragmentations of zeolite crystals were marked with red circles.

Table 1 Physicochemical properties of Pd/NaY catalysts prepared under treatment with different mechanical pressures and their catalytic performance in the indirect oxidative carbonylation of methanol to DMC.

Catalyst	S_{BET} (m^2 g^{-1})[a]	V_{micro} (cm^3 g^{-1})[a]	Size, XRD (nm)[b]	Size, TEM (nm)[c]	α (nm)[d]	Si/Al, XRD[d]	Si/Al, XPS[e]	E_a (kJ mol^{-1})[f]	TOF (s^{-1})[g]
Pd/NaY-60	893	0.32	89	370	2.463	2.8	2.8	67	0.25
Pd/NaY-150	853	0.31	84	300	2.463	2.8	2.8	67	0.22
Pd/NaY-300	841	0.30	79	270	2.464	2.7	2.7	67	0.13
Pd/NaY-450	800	0.28	64	200	2.464	2.7	2.7	58	0.11
Pd/NaY-600	732	0.26	54	180	2.464	2.7	2.7	55	0.08

[a] BET surface area, and the micropore volume determined by the *t*-plot method.

[b] Size calculated using the Scherrer equation.

[c] Size evaluated by TEM analysis.

[d] Unit cell parameter (α) determined from the (555) reflection, and the framework Si/Al molar ratio estimated from the unit cell parameter (α).

[e] Si/Al molar ratio determined from the XPS spectra.

[f] Apparent activation energy (E_a) calculated from the Arrhenius plots (Fig. S2).

[g] TOF based on the CO conversion and surface Pd atoms calculated by decreasing the CO conversion below 10 % with GHSV of 800000 mL $g_{cat.}^{-1}$ h^{-1} at 110 °C.

With increasing the mechanical pressure from 60 MPa to 300 MPa, the catalysts still had a high crystallinity (93%–98%), indicating that the mechanical compression caused a negligible damage of the zeolite framework (Fig. 2). However, the relative crystallinity was only 78% with further increasing the mechanical pressure up to 600 MPa (Fig. 2). The obvious decrease in crystallinity was attributed to the pressure-induced amorphization [15,16], suggesting that more framework defects and amorphous aluminosilicate parts were formed in the Pd/NaY-450 and Pd/NaY-600 catalysts. These five catalysts showed almost the same unit cell parameter of 2.463–2.464 nm calculated using the silicon internal standard method (Table 1) [42]. The Si/Al molar ratios measured by XRD and XPS were determined to be 2.7–2.8 on all five catalysts (Table 1), which was consistent with that of 2.8 measured by ICP-AES on the Pd/NaY catalyst before the shaping. In addition, the Bragg peaks of PdO (JCPDS 88-2434) and Pd^0 (JCPDS 01-1201) were not observed on all five catalysts (Fig. S3), which might be due to the high Pd dispersion and/or low Pd loading.

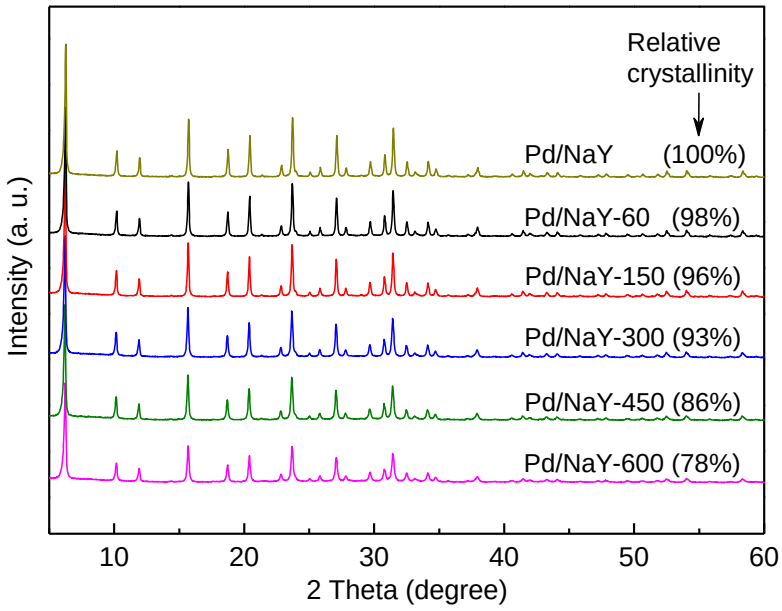

Fig. 2. XRD patterns of the Pd/NaY catalysts with the corresponding degree of crystallinity (%) prepared under treatment with different mechanical pressures.

The N_2 adsorption isotherms of all five catalysts exhibited the typical profile of microporous material (type Ⅰ) with a high adsorption capacity at low P/P_0 (Fig. 3a) [45]. All five catalysts showed similar pore size distribution consisting of micropores of about 0.74 nm corresponding to the FAU-type zeolite, and mesopores of 4.1 nm originated from the aggregation of zeolite crystals (Fig. 3b) [46]. This suggested that the mechanical compression had a negligible effect on the pore size distribution of the catalysts. As shown in Table 1, the Pd/NaY-60, -150 and -300 catalysts presented similar surface area of 841–893 $m^2\ g^{-1}$ and micropore volume of 0.30–0.32 $cm^3\ g^{-1}$. When the mechanical pressure increases to 600 MPa, the surface area and volume of the Pd/NaY-600 catalyst decreased to 732 $m^2\ g^{-1}$ and 0.26 $cm^3\ g^{-1}$, respectively. This indicated the formation of abundant framework defects and amorphous

aluminosilicate areas on the Pd/NaY-600 catalyst, which was consistent with the SEM and XRD results (Figs. 1–3 and Table 1).

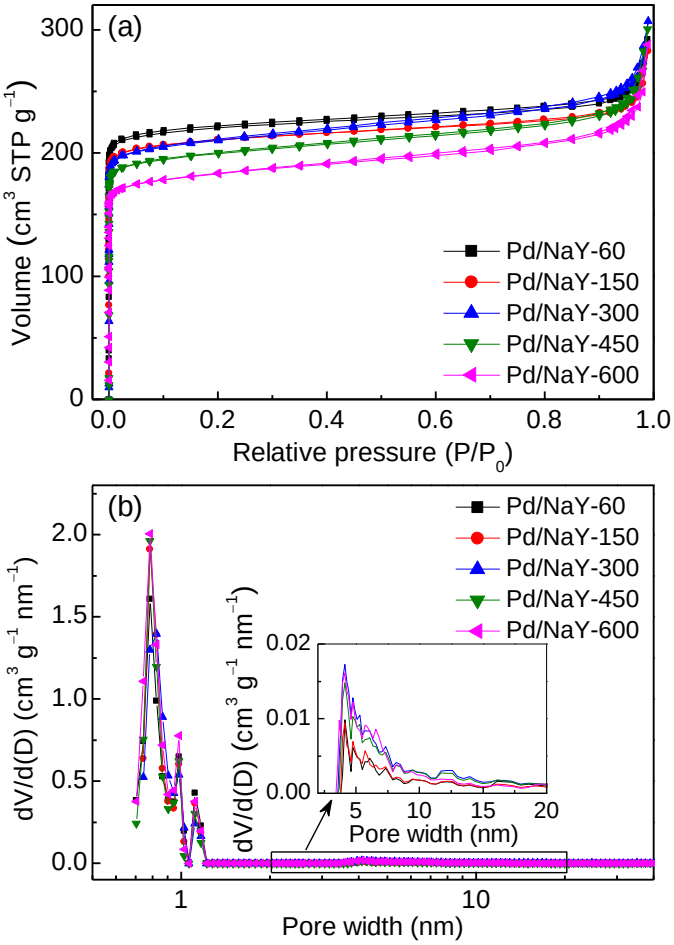

Fig. 3. (a) N_2 sorption isotherms and (b) pore size distribution of the Pd/NaY catalysts prepared under treatment with different mechanical pressures. Pore size distribution was determined by the DFT model.

The ^{29}Si CP MAS NMR spectra of the catalysts prepared under different shaping pressures were recorded to examine the structural deformation, and the results are shown in Fig. 4. The spectra of all samples contained four resonance peaks at –88, –94, –100 and –105 ppm corresponding to Q^1, Q^2, Q^3 and Q^4 species, respectively

[47,48]. The resonance peak at −88 ppm of the Pd/NaY-600 catalyst appeared with enhanced intensity in the ^{29}Si CP MAS NMR spectrum in comparison to the ^{29}Si MAS NMR (Fig. S4). The existence of H−Si dipolar interaction due to the presence of framework defects (silanols) in the Q^1 species is indicated [49−51]. As shown in Table 2, the fraction of Q^1 species was gradually increased from 7.2% to 16.7% with increasing the shaping pressure applied to the catalysts from 60 MPa to 600 MPa. This confirmed that more framework defects (Q^1 species) in the catalysts were formed under treatment at high shaping pressure, which was consistent with the XRD and N_2 sorption results.

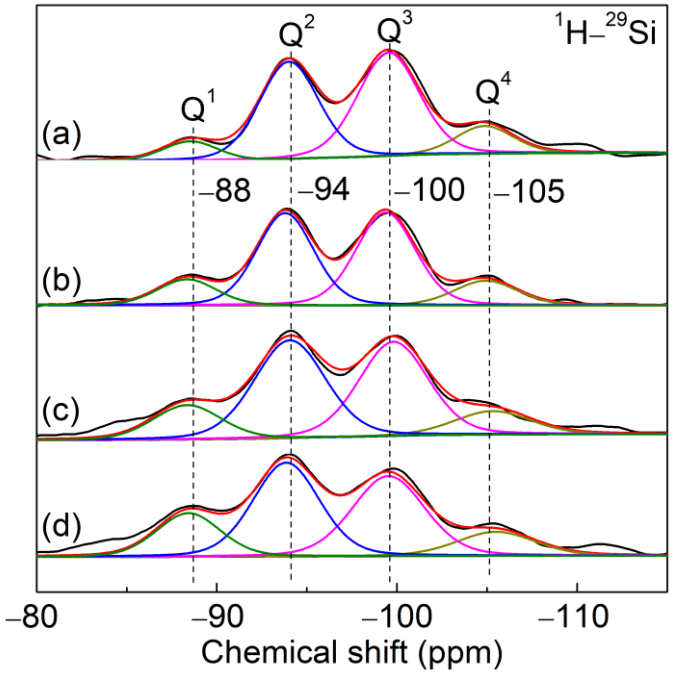

Fig. 4. Solid-state ^{29}Si CP MAS NMR spectra of the Pd/NaY catalysts prepared under treatment with different mechanical pressures: (a) Pd/NaY-60, (b) Pd/NaY-150, (c) Pd/NaY-300 and (d) Pd/NaY-600.

Table 2 Fraction of Si species of the Pd/NaY catalysts prepared under treatment with different mechanical pressures determined by solid-state ^{29}Si CP MAS NMR spectroscopic study.[a]

Catalyst	Q^1 (–88 ppm)	Q^2 (–94 ppm)	Q^3 (–100 ppm)	Q^4 (–105 ppm)
Pd/NaY-60	7.2%	38.9%	43.1%	10.8%
Pd/NaY-150	11.0%	38.0%	39.7%	11.3%
Pd/NaY-300	13.3%	39.5%	37.0%	10.2%
Pd/NaY-600	16.7%	37.4%	34.7%	11.2%

[a] Fraction of Si species determined based on the peak areas in the solid-state ^{29}Si CP MAS NMR spectra presented in Fig. 4.

3.2. Catalytic performance of Pd/NaY catalysts prepared under treatment with different mechanical pressures

The catalytic activities of the series of Pd/NaY catalysts in the indirect oxidative carbonylation of methanol to DMC are presented in Fig. 5. When the mechanical pressure was less than 300 MPa, the CO conversion of about 90.4% was preserved while the DMC selectivity increased progressively from 74.4% to 80.4%. At the

mechanical pressure larger than 300 MPa, the CO conversion declined from 90.4% to 78.3% while the DMC selectivity of about 80% was preserved. In addition, the DMC selectivity using the Pd/NaY-60, -150, -300, -450 and -600 catalysts gradually increased, while the selectivity of methyl formate, dimethoxymethane byproducts progressively decreased with prolonging the reaction time from 1 h to 6 h (Fig. S5). For example, the selectivities of DMC, methyl formate and dimethoxymethane were 75.7%, 13.7% and 10.6% after 1 h catalytic test, respectively. After 6 h, the selectivities of DMC, methyl formate and dimethoxymethane using the Pd/NaY-300 catalyst were 80.4%, 10.9% and 8.6%, respectively (Fig. S5). The increase of DMC selectivity with prolonging the reaction time would be discussed in posterior XPS analysis.

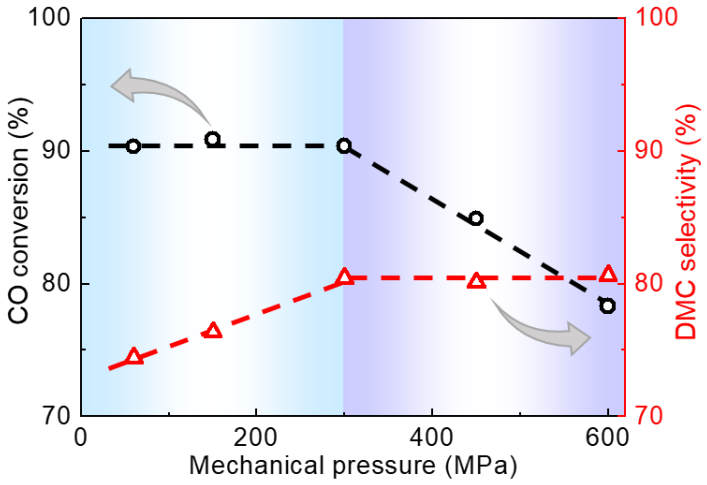

Fig. 5. CO conversion (black circles) and DMC selectivity (red triangles) for the indirect oxidative carbonylation of methanol to DMC on the Pd/NaY catalysts prepared under treatment with different mechanical pressures (60, 150, 300, 450 and 600 MPa). Reaction conditions: 0.1000 g catalyst; feed gas, $CO/CH_3ONO/N_2$ =

1/6/33 (mole); GHSV = 8000 mL $g_{cat.}^{-1}$ h^{-1}; reaction temperature = 110 ºC; feed pressure = 0.1 MPa. The data were collected after 6 h catalytic test (each point was an average value of three measurements).

To study both internal and external diffusion, the kinetic experiments were conducted, and the results are shown in Fig. S6 and Table S1. The GHSV was in the range of 4000–24000 mL $g_{cat.}^{-1}$ h^{-1} for the Pd/NaY-300 catalyst with different amounts of 0.1000 g and 0.1600 g; a similar CO conversion under the same GHSV was measured (Fig. S6). This suggested that the external diffusion effect could be neglected with a GHSV larger than 4000 mL $g_{cat.}^{-1}$ h^{-1} [52,53]. The Thiele modulus was determined to be 0.156, 0.126, 0.113, 0.086 and 0.075 for the Pd/NaY-60, -150, -300, -450 and -600 catalysts, respectively (Table S1 and details are provided in SI). All the effectiveness factors approached the value of 1 and thus the DMC synthesis could be regarded as surface-limited reaction (Table S1) [54,55]. In addition, a thermocouple was placed in the middle of the catalyst bed for monitoring the reaction temperature during the catalytic tests, and no temperature rise (< 1 ºC) was detected between the catalyst bed and the reactor during the kinetic experiments. Therefore, the heat and mass transfer should have a negligible effect on the reaction rate.

The apparent activation energies for the indirect oxidative carbonylation of methanol to DMC were measured in the temperature range of 100–120 ºC with an

interval of 5 ºC. As presented in Table 1, these five Pd/NaY catalysts showed comparable apparent activation energies of 55–67 kJ mol^{-1} under the same reaction conditions (Fig. S2). This indicated that the dominant reaction pathway and the rate control step were identical for these catalysts [56,57]. Furthermore, the CO conversion was decreased below 10% at 110 ºC and GHSV of 800000 mL $g_{cat.}^{-1}$ h^{-1} (details provided in SI). The intrinsic activity, i.e. the TOF decreased from 0.25 s^{-1} to 0.08 s^{-1}, with increasing the shaping pressure from 60 MPa to 600 MPa (Table 1). This was possibly related to the amorphization of zeolite support after the mechanical treatment.

3.3. Understanding the formation of mechanical pressure-mediated active sites in Pd/NaY catalysts

TEM study of the used Pd/NaY catalysts prepared under treatment with different mechanical pressures was conducted to evaluate the size and distribution of palladium. As described previously, the Pd/NaY catalyst was prepared by an ion-exchange method with Pd precursor of $Pd(NH_3)_4^{2+}$; and the low-temperature calcination at 200 ºC caused the $Pd(NH_3)_4^{2+}$ to lose partially the NH_3 ligands and to generate the $Pd(NH_3)_n^{2+}$ ($n < 2$) sites on the catalyst [41]. Neither Pd clusters (below 2 nm) nor nanoparticles were observed on the fresh Pd/NaY-60 catalyst before the catalytic test (Fig. S7). While the used Pd/NaY-60 catalyst after 6 h test contained a mixture of both small Pd clusters (about 1 nm) and large Pd nanoparticles (Fig. 6a1,a2). The average

size of the Pd nanoparticles was estimated to be 13.1 nm based on measuring about 200 nanoparticles (*inset* of Fig. 6a1). The TEM images of fresh and used Pd/NaY-60 catalysts indicated that the large Pd nanoparticles were formed because of the catalytic test. This was in line with the previous observation revealing the palladium sintering on the Pd/NaY catalyst after the catalytic test [41]. The used Pd/NaY-150 catalyst contained Pd nanoparticles of 6.3 nm that were remarkably smaller than the counterparts on the Pd/NaY-60 catalyst (Fig. 6a1,b1). Interestingly, no big Pd nanoparticles were detected on the used Pd/NaY-300 catalyst and only mono-dispersed Pd clusters of about 1 nm confined within the zeolite framework were identified (Fig. 6c1,c2). The used Pd/NaY-450 was similar to the used Pd/NaY-300 catalyst with the exception that sporadic large Pd nanoparticles of about 20 nm could be seen in the TEM pictures (Fig. 6c1,d1). Bigger Pd particles up to 110 nm were detected on the used Pd/NaY-600 catalyst (Fig. 6e1). The XRD pattern of this sample contained the Bragg peaks corresponding to the metallic Pd^0(111) and Pd^0(200) (JCPDS 01-1201) with a non-homogeneous dispersion (Fig. S3). As stated above, the mechanical compression resulted in the formation of framework defects, such as collapse of micropore, framework distortions, fragmentation of primary zeolite crystals, and even amorphization of zeolites (Table 1) [16,19]. With increasing the mechanical pressure from 60 MPa to 300 MPa, the average size of the Pd nanoparticles decreased from 13.1 nm to 6.3 nm, but only mono-dispersed Pd clusters (about 1 nm) were detected on the Pd/NaY-300 catalyst (Fig. 6a1–c1,a2–c2). It was

thus reasonable to infer that the framework defects possibly played an important role in hindering the aggregation of Pd clusters. This was in line with the report disclosing that the zeolite defects served as hosting place for the Pd species, thus separating them from each other and preventing their growth [58–60]. At the mechanical pressure larger than 300 MPa, more amorphous aluminosilicate areas were formed, and thus possibly led to sintering of the Pd and formation of bigger metal particles (Fig. 6e1) [35,58].

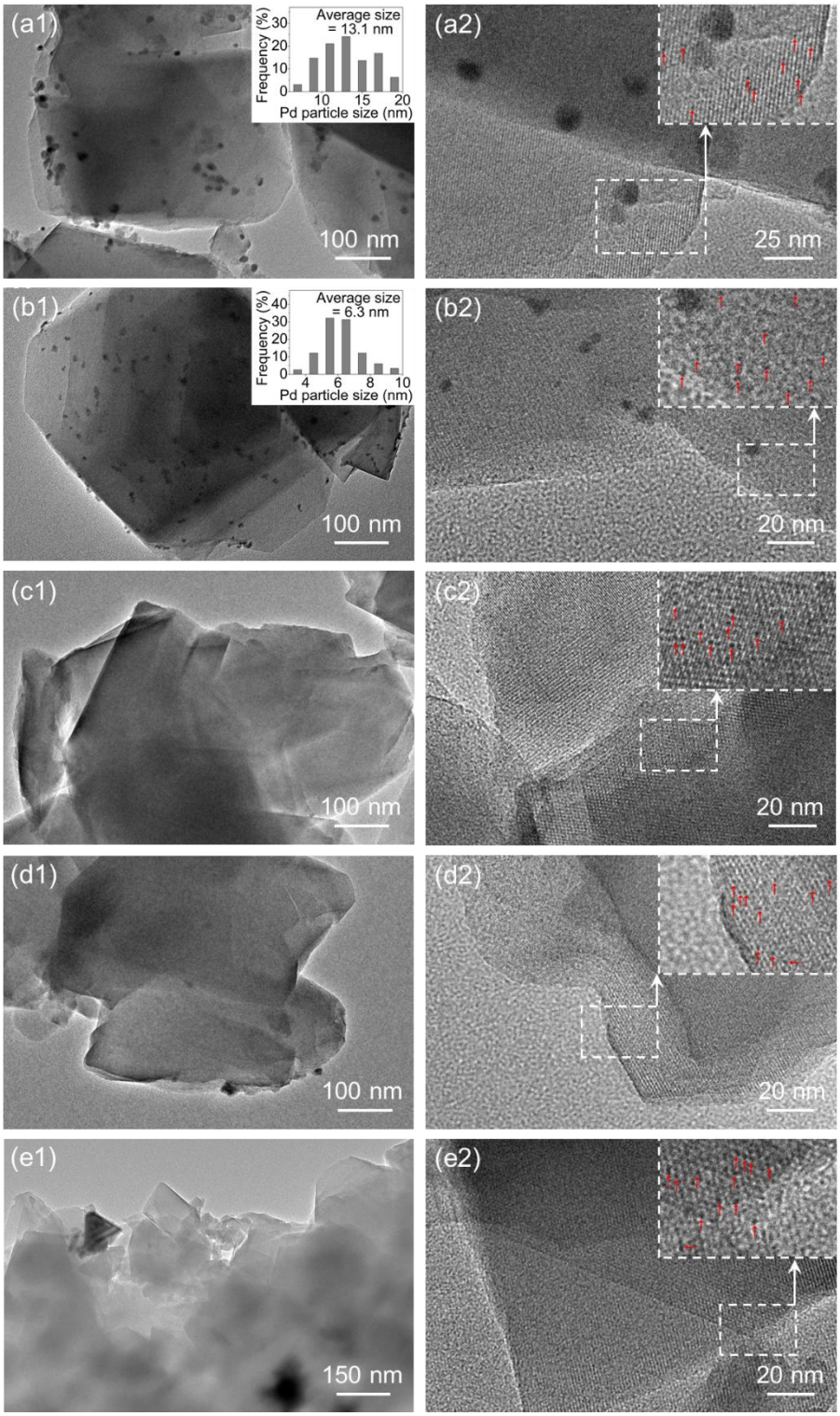

Fig. 6. TEM images of the used catalysts after 6 h catalytic test: (a1,a2) Pd/NaY-60, (b1,b2) Pd/NaY-150, (c1,c2) Pd/NaY-300, (d1,d2) Pd/NaY-450 and (e1,e2) Pd/NaY-600. *Inset* of (a1) and (b1): size distribution of Pd nanoparticles determined by measuring about 200 nanoparticles. *Inset* of (a2), (b2), (c2), (d2) and (e2): enlarged

area of the catalysts and Pd clusters marked by red arrows.

Consistent with the TEM observation, the HAADF-STEM images of the used Pd/NaY-300 catalyst further confirmed the presence of mono-dispersed Pd clusters (Figs. 6c1,c2 and 7). The average size of the Pd clusters was determined to be 1.3 nm based on measuring about 200 clusters (*inset* of Fig. 7a). The HAADF-STEM-EDS elemental mapping showed that the Pd was homogeneously distributed on the used Pd/NaY-300 catalyst.

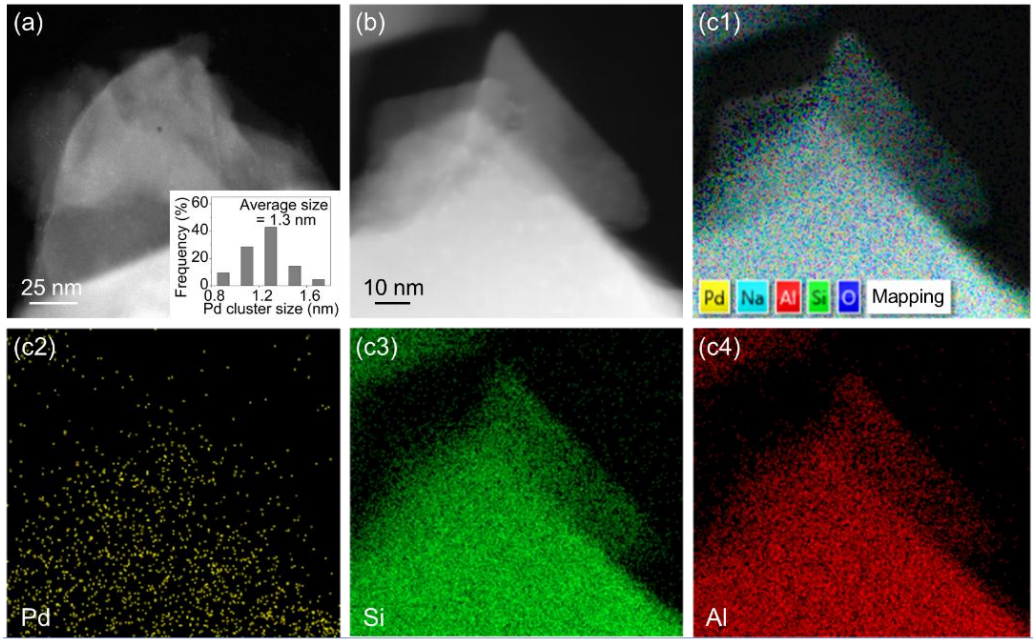

Fig. 7. (a) HAADF-STEM image and the size distribution of Pd (*inset*), (b) HAADF-STEM image and (c1–c4) the corresponding HAADF-STEM-EDS elemental mapping of the used Pd/NaY-300 catalyst after 6 h catalytic test. The size distribution of Pd determined by measuring about 200 clusters.

As stated above, the Pd^{2+} species were generally believed to be the active sites for

the formation of DMC [35,39]. Therefore, XPS study was performed to check the effect of mechanical pressure on the electronic properties of Pd species. As shown in Fig. 8A, the XPS spectra confirmed the presence of Pd, Si, Al, Na, O and C elements on all five catalysts. The Pd 3d regions of these catalysts exhibited the $3d_{5/2}$ and $3d_{3/2}$ peaks with a spin-orbit splitting of 5.3 eV; only the Pd $3d_{5/2}$ peak was discussed herein (Fig. 8). Generally, Pd^0 was characterized by a Pd $3d_{5/2}$ peak at 334.8–335.6 eV, and it shifted to higher binding energy with the increase of palladium oxidation state. The peaks detected at 336.4–337.3 eV and 338.0–338.9 eV corresponded to the Pd^{2+} and Pd^{4+} species, respectively [57,61–64]. Consequently, the peaks at 336.1 eV and 338.0 eV were assigned to $Pd^{\delta+}$ and $Pd^{(2+\delta)+}$ species ($0 < \delta \leq 2$) on all five catalysts (Fig. 8B); similar observations had been reported previously [65,66]. The XPS peak area ratio corresponding to the $Pd^{(2+\delta)+}/Pd^{\delta+}$ species for these five catalysts decreased remarkably from 1.16 to 0.45 with increasing the mechanical pressure from 60 MPa to 600 MPa applied to the catalysts (Table 3). Generally, the charge of Pd species increases with decreasing the particle size based on the intrinsic size effect [61,67]. Herein, the average Pd charge monotonically decreased with increasing the mechanical pressure (Table 3), while the Pd particle size distribution showed a volcano-like behavior according to the TEM observations (Fig. 6). The lack of correlation between the Pd particle size and the charge could be explained as follows: (1) The $Pd^{(2+\delta)+}$ species possibly result from the Pd clusters and nanoparticles charged by the zeolite framework through the formation of Pd–O ionic bonds [35,40] and (2)

Lewis acid sites of zeolite support are considered to be electron acceptors and thus make the Pd species lose the electrons [34]. The increase of the mechanical pressure caused the formation of more framework defects and partial amorphization, which inhibited the formation of the $Pd^{(2+\delta)+}$ species and thus decreased the $Pd^{(2+\delta)+}/Pd^{\delta+}$ ratio [68].

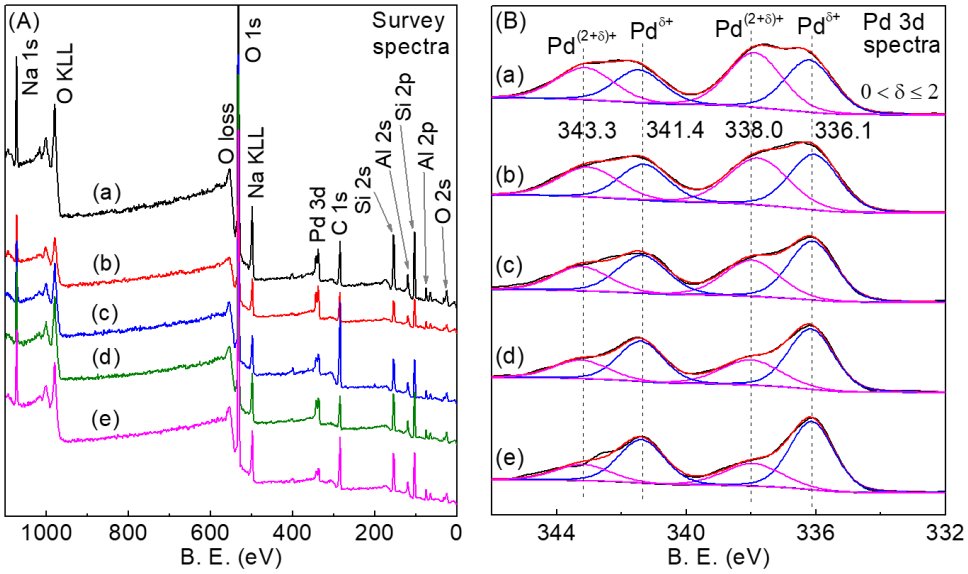

Fig. 8. (A) XPS spectra and (B) Pd 3d spectra of used catalysts after 6 h catalytic test: (a) Pd/NaY-60, (b) Pd/NaY-150, (c) Pd/NaY-300, (d) Pd/NaY-450 and (e) Pd/NaY-600.

Table 3 Peak areas of $Pd^{\delta+}$ ($0 < \delta \leq 2$), $Pd^{(2+\delta)+}$, and $Pd^{(2+\delta)+}/Pd^{\delta+}$ area ratio of used catalysts after 1 h and 6 h catalytic tests determined by XPS.[a]

Catalyst	Time	Area of $Pd^{\delta+}$	Area of $Pd^{(2+\delta)+}$	$Pd^{(2+\delta)+}/Pd^{\delta+}$ ratio
Pd/NaY-60	1 h	5744	10037	1.75
Pd/NaY-150	1 h	8660	11574	1.34

Pd/NaY-300	1 h	9110	7506	0.82
Pd/NaY-450	1 h	8448	5877	0.70
Pd/NaY-600	1 h	9678	5269	0.54
Pd/NaY-60	6 h	7761	8982	1.16
Pd/NaY-150	6 h	8428	8693	1.03
Pd/NaY-300	6 h	8728	6453	0.74
Pd/NaY-450	6 h	8409	4672	0.56
Pd/NaY-600	6 h	10281	4578	0.45

[a] Peak areas of $Pd^{(2+\delta)+}$ at 338.0 eV and $Pd^{\delta+}$ at 336.1 eV based on XPS spectra of the used catalysts after 1 h (Fig. S8) and 6 h (Fig. 8) tests.

The XPS results and catalytic performance of these five catalysts after 6 h catalytic test showed that the area ratio of $Pd^{(2+\delta)+}/Pd^{\delta+}$ decreased gradually, while the DMC selectivity increased with raising the mechanical pressure from 60 MPa to 600 MPa (Figs. 5 and 8, Table 3). As stated above, the DMC selectivity also increased on each catalyst with extending the reaction time from 1 h to 6 h (Fig. S5). The $Pd^{(2+\delta)+}/Pd^{\delta+}$ area ratios of catalysts Pd/NaY-60, -150, -300, -450 and -600 after 6 h test were smaller than the ones measured after 1 h (Table 3). The relationship between the $Pd^{(2+\delta)+}/Pd^{\delta+}$ ratio and DMC selectivity on these five catalysts after 1 h and 6 h catalytic tests was shown in Fig. 9. A linear relationship with a correlation coefficient $R^2 = 0.9$ between the DMC selectivity and the $Pd^{(2+\delta)+}/Pd^{\delta+}$ ratio was observed (Fig.

9). This indicated that the $Pd^{(2+\delta)+}/Pd^{\delta+}$ ratio played a critical role in the DMC selectivity which would be further discussed in posterior Section 3.4.

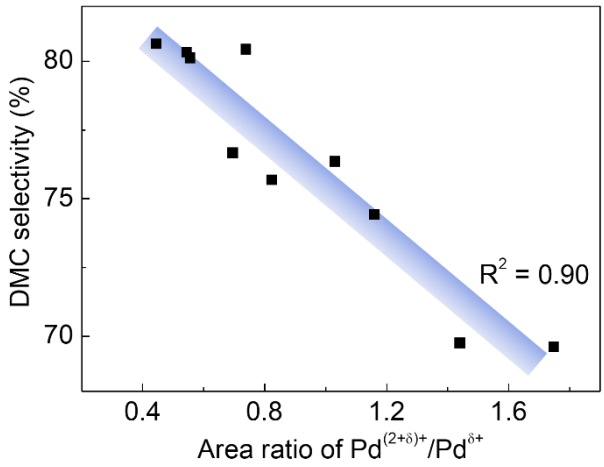

Fig. 9. The relationship between the area ratio of $Pd^{(2+\delta)+}/Pd^{\delta+}$ and DMC selectivity of the used catalysts (Pd/NaY-60, -150, -300, -450 and -600) after 1 h and 6 h catalytic tests ($Pd^{(2+\delta)+}/Pd^{\delta+}$ ratio shown in Table 3).

Combining the TEM and XPS results, it could be concluded that the highly dispersed Pd species contributed to the high CO conversion, while the low $Pd^{(2+\delta)+}/Pd^{\delta+}$ ratio led to the high DMC selectivity for the indirect oxidative carbonylation of methanol to DMC.

3.4. Correlation between the $Pd^{(2+\delta)+}/Pd^{\delta+}$ ratio and DMC selectivity: Enhanced adsorption of reactants

Carbon monoxide is not only a common probe molecule but also the reactant for the DMC synthesis. The DRIFTS spectra of CO adsorbed on the used Pd/NaY catalysts were presented in Fig. 10. The band at 2103 cm^{-1} was assigned to the linear

CO adsorption over $Pd^{\delta+}$ species ($0 < \delta \leq 2$), and the band at 2140 cm^{-1} corresponded to the linear CO adsorption on $Pd^{(2+\delta)+}$ species [69,70]. With increasing the mechanical pressure of the catalysts from 60 MPa to 600 MPa, the band corresponding to $Pd^{(2+\delta)+}$ species declined while the band related with $Pd^{\delta+}$ species gradually increased (Fig. 10a). This was consistent with the evolution of the $Pd^{(2+\delta)+}/Pd^{\delta+}$ ratio determined by XPS (Fig. 8 and Table 3). When the temperature of the DRIFTS reaction cell was increased from 30 ºC to 50 ºC, the band corresponding to $Pd^{(2+\delta)+}$ species decreased noticeably while the intensity of the band corresponding to $Pd^{\delta+}$ species was well preserved. This suggested that CO adsorption on the $Pd^{(2+\delta)+}$ species was weaker than on the $Pd^{\delta+}$ species, which was due to the weak π back-donation [57]. This finding further indicated that the change of the $Pd^{(2+\delta)+}/Pd^{\delta+}$ ratio could affect the adsorption of CO reactant on these catalysts.

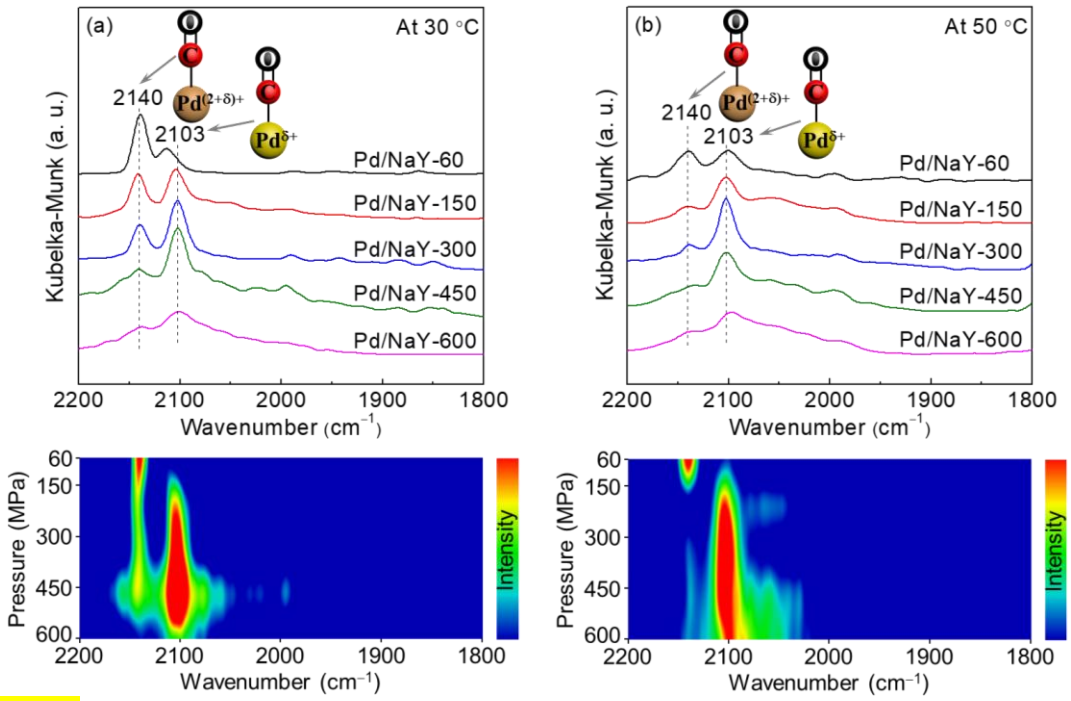

Fig. 10. DRIFTS spectra of CO adsorbed on the used Pd/NaY-60, -150, -300, -450

and -600 catalysts after 6 h catalytic test at (a) 30 ºC and (b) 50 ºC. The samples were pre-treated in N_2 at 200 ºC, cooled down to 30 ºC, exposed to 10 vol% CO in N_2 and thoroughly purged with N_2. After that, the spectra were obtained at 30 ºC and 50 ºC.

In order to further understand the effect of the $Pd^{(2+\delta)+}/Pd^{\delta+}$ ratio on the DMC selectivity, we conducted DFT calculations to probe the adsorption of CO and CH_3ONO reactants on the Pd species with different valence states. A primitive cell ($Si_{24}Al_{24}O_{96}$) of the faujasite structure with the $Fd\bar{3}$ space group symmetry was used to model the NaY zeolite. Based on the Löwenstein rule, we replaced 12 Al atoms by 12 Si atoms to obtain a Si/Al molar ratio of 3.0, which was close to that of the synthesized Pd/NaY catalyst (Si/Al=2.8, Table 1). Furthermore, 12 Na atoms were added into the cell based on the reported distribution, i.e., 17% in site Ⅰ (~2 Na atoms), 29% in site I' (~4 Na atoms) and 54% in site Ⅱ (~6 Na atoms) [71,72]. A Pd_{13} cluster reported by a previous study [37] was embedded into the supercage of NaY (Pd_{13}@NaY) to model the synthesized Pd/NaY catalysts and the optimized structure was shown in Fig. 11a. Since the synthesized Pd/NaY catalysts had mixed valence states of (2+δ)+ and δ+, we also constructed $Pd_{13}O_8$@NaY and $Pd_{13}O_{10}$@NaY models by adding eight or ten oxygen atoms onto the Pd_{13} cluster of Pd_{13}@NaY (Fig. 11). To locate the stable structures of $Pd_{13}O_8$@NaY and $Pd_{13}O_{10}$@NaY, we carried out a molecular dynamics (MD) simulation of ~ 25 ps (time step: 1 fs) on each of these two systems in the canonical (NVT) ensemble with T = 137 ºC. For each system,

geometry optimizations were performed on the selected low-energy structures obtained from the MD simulation, and the structure with the lowest energy was selected for further study. Charge analyses showed that the Pd atoms of Pd_{13}@NaY were partially transformed into $Pd^{(2+\delta)+}$ species after adding eight or ten oxygen atoms onto the Pd_{13} cluster (Table S2). The $Pd_{13}O_{10}$@NaY had the highest $Pd^{(2+\delta)+}/Pd^{\delta+}$ ratio, followed by $Pd_{13}O_8$@NaY and then Pd_{13}@NaY (Table S2).

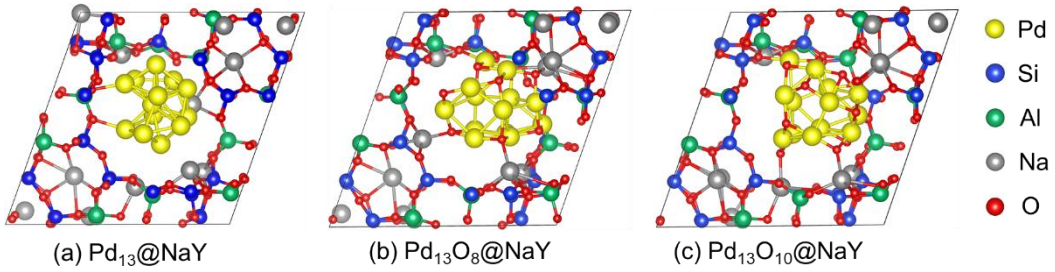

Fig. 11. Optimized structures of (a) Pd_{13}, (b) $Pd_{13}O_8$, and (c) $Pd_{13}O_{10}$ clusters embedded in the supercage of NaY zeolite. Pd, Si, Al, Na, and O atoms were presented in yellow, blue, green, grey, and red, respectively.

Since the DRIFTS spectra suggested linear adsorption of CO on all five Pd/NaY catalysts (Fig. 10), only the top-site adsorption was considered in our DFT calculations. The optimized structures of linear adsorption of CO on the Pd_{13}@NaY, $Pd_{13}O_8$@NaY, and $Pd_{13}O_{10}$@NaY models are presented in Fig. S9. We found that the CO preferred to be adsorbed on the $Pd^{\delta+}$ sites in comparison with the $Pd^{(2+\delta)+}$ sites (Table 4). This was mainly due to the stronger π back-donation of $Pd^{\delta+}$ compared to the $Pd^{(2+\delta)+}$ sites, [57] which was consistent with the DRIFTS results (Fig. 10). The most favorable adsorption energy of CO at $Pd^{\delta+}$ site increased significantly with

decreasing the oxygen atoms of the models (1.32 eV for $Pd_{13}O_{10}$@NaY → 2.06 eV for $Pd_{13}O_8$@NaY → 2.61 eV for Pd_{13}@NaY, Table 4) [73]. In addition, the dissociative adsorption of CH_3ONO on the considered models showed a similar trend to the adsorption of the CO reactant. More specifically, the dissociative adsorption energies of CH_3ONO on the $Pd_{13}O_{10}$@NaY, $Pd_{13}O_8$@NaY, and Pd_{13}@NaY models were 2.06, 2.44, and 2.71 eV, respectively (Fig. S9 and Table S3). Therefore, our DFT results suggested that the lower the $Pd^{(2+\delta)+}/Pd^{\delta+}$ ratio of the catalyst was, the stronger the adsorption of CO and CH_3ONO reactants were expected.

Table 4 Calculated most favorable adsorption of CO at the $Pd^{\delta+}$ and $Pd^{(2+\delta)+}$ sites in the Pd_{13}@NaY, $Pd_{13}O_8$@NaY, and $Pd_{13}O_{10}$@NaY models.

Model	Adsorption mode	Site[a]	Valence state[b]	E_{ads} (eV)[c]
$Pd_{13}O_{10}$@NaY	Linear	Pd-13	δ+	1.32
	Linear	Pd-6	(2+δ)+	0.64
$Pd_{13}O_8$@NaY	Linear	Pd-3	δ+	2.06
	Linear	Pd-4	(2+δ)+	0.46
Pd_{13}@NaY	Linear	Pd-13	δ+	2.61

[a] Pd-*x*, where *x* represents the number of Pd atoms in the models (Fig. S9).

[b] The valence states of Pd were determined by calculating their Bader charges (see Table S2 in SI for details).

[c] Calculated adsorption energy (E_{ads}) of CO.

The calculated high adsorption energies of CO and CH_3ONO also suggested that these two reactants could be easily adsorbed on the Pd/NaY catalysts (Tables 3 and S2) [73]. This indirectly indicated that the Langmuir-Hinshelwood mechanism was preferred for the DMC synthesis over the Pd/NaY catalysts [40,74]. Since DMC synthesis and catalytic decomposition of CH_3ONO reactant were parallel competing reactions (details provided in SI), the catalytic decomposition of CH_3ONO was examined on all five Pd/NaY catalysts at 110 ºC using a feed of CH_3ONO/N_2 = 1/4 (mole). With increasing the shaping pressure from 60 MPa to 600 MPa, the activity of undesired decomposition of CH_3ONO reactant gradually decreased from 30.0% to 20.9% (GHSV = 30000 mL $g_{cat.}^{-1}$ h^{-1}) and from 21.7% to 15.2% (GHSV = 90000 mL $g_{cat.}^{-1}$ h^{-1}) on these five Pd/NaY catalysts, which gave a reverse trend to the DMC selectivity for the DMC synthesis (Figs. 5 and S10). This suggested that Pd/NaY catalyst with a low $Pd^{(2+\delta)+}/Pd^{\delta+}$ ratio could hinder the undesired decomposition of CH_3ONO reactant.

In summary, combining the XPS, DRIFTS and DFT results, it could be concluded that the mechanical pressure tuned the $Pd^{(2+\delta)+}/Pd^{\delta+}$ ratio and further adjusted the adsorption of CO and CH_3ONO reactants. The increased amount of $Pd^{\delta+}$ species could enhance the adsorption of CO and CH_3ONO reactants and inhibit the undesired decomposition of CH_3ONO reactant into byproducts, thereby improving the DMC selectivity.

3.5. Stability of the Pd/NaY-300 catalyst

A long-term catalytic test was carried out on the best performing Pd/NaY-300 catalyst, and the results are shown in Fig. 12. The catalyst showed a good stability throughout the 150 h catalytic test, exhibiting CO conversion of 89 ± 2%, CH_3ONO conversion of 37 ± 3%, and DMC selectivity of 83 ± 1%. The DMC selectivity gradually increased with extending the reaction time from 1 h to 150 h (Fig. 12). The $Pd^{(2+\delta)+}/Pd^{\delta+}$ area ratio of the Pd/NaY-300 catalyst after 150 h catalytic test was determined to be 0.40 by XPS (Fig. S11). According to the nearly linear relationship between the $Pd^{(2+\delta)+}/Pd^{\delta+}$ ratio and DMC selectivity (Fig. 9), the predicted DMC selectivity was 81%. This further confirmed that the DMC selectivity depended on $Pd^{(2+\delta)+}/Pd^{\delta+}$ ratio. The TEM revealed that the used Pd/NaY-300 catalyst after 150 h contained a mixture of both abundant Pd clusters of about 1 nm and sporadic Pd nanoparticles of about 6 nm (Fig. S12). Except sporadic Pd nanoparticles, the TEM images of the used Pd/NaY-300 catalyst (after 150 h catalytic test) were similar to the catalyst after 6 h catalytic test (Figs. 6c1,c2 and S12), which indicated the excellent resistance to Pd sintering. No Bragg peaks corresponding to PdO (JCPDS 88-2434) and Pd^0 (JCPDS 01-1201) were detected in the XRD pattern of the used Pd/NaY-300 catalyst (Fig. S13).

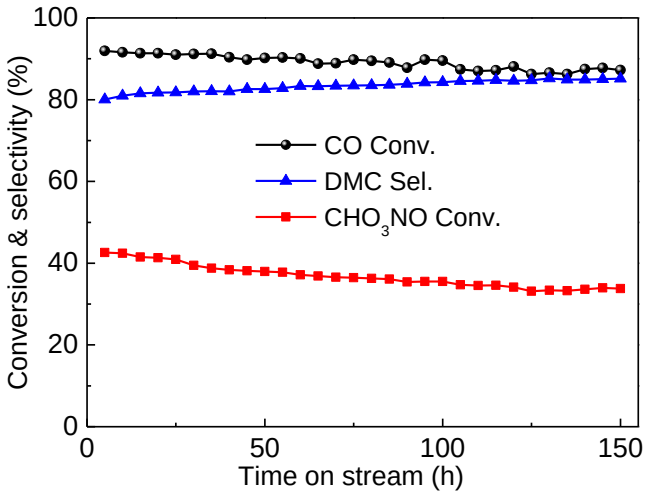

Fig. 12. Durability performance of the Pd/NaY-300 catalyst in the indirect oxidative carbonylation of methanol to DMC measured for 150 h. Reaction conditions: 0.1000 g catalyst; feed gas, $CO/CH_3ONO/N_2$ = 1/6/33 (mole); GHSV = 8000 mL $g_{cat.}^{-1}$ h^{-1}; reaction temperature = 110 ºC; feed pressure = 0.1 MPa. Each point was an average value of three measurements.

4. Conclusions

Palladium-containing NaY zeolite catalysts were prepared by mechanical-pressure controlled treatment and tested in the indirect oxidative carbonylation of methanol to dimethyl carbonate (DMC). The mechanical pressure applied to the Pd/NaY catalysts was found to have a pronounced effect on the Pd dispersion and the catalysts stability. The Pd clusters with a size of 1.3 nm homogeneously distributed in the NaY zeolite were obtained under mechanical-pressure treatment of 300 MPa. This catalyst not only showed the high CO conversion of 89% and DMC selectivity of 83%, but also was very stable for at least 150 h. The DMC selectivity was closely related to the

mechanical pressure applied as it was related with the amount of $Pd^{(2+\delta)+}$ and $Pd^{\delta+}$ ($0 < \delta \leq 2$) active sites formed in the Pd/NaY catalysts. The *in situ* DRIFTS and DFT calculations revealed clearly that the $Pd^{\delta+}$ in contrast to $Pd^{(2+\delta)+}$ species enhanced the adsorption of CO and CH_3ONO reactants and inhibited the undesired decomposition of CH_3ONO reactant into byproducts, and thus enhanced the DMC selectivity.

Declaration of Competing Interest

The authors declare that they have no known competing financial interests or personal relationships that could have appeared to influence the work reported in this paper.

Acknowledgements

This work was supported by the National Natural Science Foundation of China (21908246, 21975285, 21991090, 21991091), Shanghai Sailing Program (20YF1410000), Fundamental Research Funds for the Central Universities (18CX02148A) and the Sino-French International Laboratory (LIA) “Zeolites”.

References

[1] S. Mitchell, N. Michels, J. Pérez-Ramírez, Chem. Soc. Rev. 42 (2013) 6094–6112.

[2] J. Zhou, J. Teng, L. Ren, Y. Wang, Z. Liu, W. Liu, W. Yang, Z. Xie, J. Catal. 340 (2016) 166–176.

[3] G.T. Whiting, S. Chung, D. Stosic, A.D. Chowdhury, L.I. van der Wal, D. Fu, J.

Zecevic, A. Travert, K. Houben, M. Baldus, B.M. Weckhuysen, ACS Catal. 9 (2019) 4792–4803.

[4] S.Y. Devyatkov, A.A. Zinnurova, A. Aho, D. Kronlund, J. Peltonen, N.V. Kuzichkin, N.V. Lisitsyn, D.Y. Murzin, Ind. Eng. Chem. Res. 55 (2016) 6595–6606.

[5] A. Carne-Sanchez, I. Imaz, M. Cano-Sarabia, D. Maspoch, Nat. Chem. 5 (2013) 203–211.

[6] N. Michels, S. Mitchell, J. Pérez-Ramírez, ACS Catal. 4 (2014) 2409–2417.

[7] V.G. Baldovino-Medrano, B. Kartheuser, E.M. Gaigneaux, Catal. Today 338 (2019) 81–92.

[8] T. Shoinkhorova, A. Dikhtiarenko, A. Ramirez, A. Dutta Chowdhury, M. Caglayan, J. Vittenet, A. Bendjeriou-Sedjerari, O.S. Ali, I. Morales-Osorio, W. Xu, J. Gascon, ACS Appl. Mater. Inter. 11 (2019) 44133–44143.

[9] G. Ertl, H. Knözinger, F. Schüth, J. Weitkamp, Handbook of Heterogeneous Catalysis, Wiley-VCH, Weinheim, 2008, p. 690–694.

[10] L.F. Bobadilla, A. Muñoz-Murillo, O.H. Laguna, M.A. Centeno, J.A. Odriozola, Chem. Eng. J. 357 (2019) 248–257.

[11] V.G. Baldovino-Medrano, C. Alcázar, M.T. Colomer, R. Moreno, E.M. Gaigneaux, Appl. Catal. A 468 (2013) 190–203.

[12] D. Seoung, Y. Lee, H. Cynn, C. Park, K. Choi, D.A. Blom, W.J. Evans, C. Kao, T. Vogt, Y. Lee, Nat. Chem. 6 (2014) 835–839.

[13] D. Kim, Y. Lee, Y. Kim, K. Mingle, J. Lauterbach, D.A. Blom, T. Vogt, Y. Lee, Chem. Eur. J. 24 (2018) 1041−1045.

[14] G.L. Hill, E. Bailey, M.C. Stennett, N.C. Hyatt, E.M. Maddrell, P.F. McMillan, J.A. Hriljac, J. Am. Chem. Soc. 133 (2011) 13883−13885.

[15] M.B. Kruger, R. Jeanloz, Science 249 (1990) 647−649.

[16] J.S. Tse, D.D. Klug, J.A. Ripmeester, S. Desgreniers, K. Lagarec, Nature 369 (1994) 724−727.

[17] D. Seoung, Y. Lee, S.J. Kim, H. Lee, D. Ahn, N. Shin, T. Vogt, Y. Lee, Microporous Mesoporous Mater. 136 (2010) 75−82.

[18] Y. Lee, T. Vogt, J.A. Hriljac, J.B. Parise, J.C. Hanson, S.J. Kim, Nature 420 (2002) 485−489.

[19] Y. Lee, S.J. Kim, C. Kao, T. Vogt, J. Am. Chem. Soc. 130 (2008) 2842−2850.

[20] J.L. Jordá, F. Rey, G. Sastre, S. Valencia, M. Palomino, A. Corma, A. Segura, D. Errandonea, R. Lacomba, F.J. Manjón, Ó. Gomis, A.K. Kleppe, A.P. Jephcoat, M. Amboage, J.A. Rodríguez-Velamazán, Angew. Chem. Int. Ed. 52 (2013) 10458−10462.

[21] W. Zhou, K. Cheng, J. Kang, C. Zhou, V. Subramanian, Q. Zhang, Y. Wang, Chem. Soc. Rev. 48 (2019) 3193−3228.

[22] J. Bao, G. Yang, Y. Yoneyama, N. Tsubaki, ACS Catal. 9 (2019) 3026−3053.

[23] P. Chen, G. Zhao, X.R. Shi, J. Zhu, J. Ding, Y. Lu, iScience 17 (2019) 315−324.

[24] G. Fiorani, A. Perosa, M. Selva, Green Chem. 20 (2018) 288–322.

[25] A.A. Marciniak, O.C. Alves, L.G. Appel, C.J.A. Mota, J. Catal. 371 (2019) 88–95.

[26] K. Xuan, Y. Pu, F. Li, J. Luo, N. Zhao, F. Xiao, Chin. J. Catal. 40 (2019) 553–566.

[27] P. Kumar, V.C. Srivastava, U.L. Štangar, B. Mušič, I.M. Mishra, Y. Meng, Catal. Rev. (2019) DOI: 10.1080/01614940.2019.1696609.

[28] Z. Wang, M. Zhang, X. Hu, V.P. Dravid, Z. Xu, G. Guo, Chem. Commun. 56 (2020) 403–406.

[29] J. Zhao, R. Shi, Y. Quan, J. Liu, J. Wang, Y. Pei, X. Wang, Z. Li, J. Ren, Chem. Eng. Sci. 207 (2019) 1060−1071.

[30] S. Huang, B. Yan, S. Wang, X. Ma, Chem. Soc. Rev. 44 (2015) 3079–3116.

[31] S. Uchiumi, K. Ataka, T. Matsuzaki, J. Organomet. Chem. 576 (1999) 279–289.

[32] N. Keller, G. Rebmann, V. Keller, J. Mol. Catal. A: Chem. 317 (2010) 1–18.

[33] H. Tan, Z. Wang, Z. Xu, J. Sun, Y. Xu, Q. Chen, Y. Chen, G. Guo, Catal. Today 316 (2018) 2–12.

[34] Y. Dong, S. Huang, S. Wang, Y. Zhao, J. Gong, X. Ma, ChemCatChem 5 (2013) 2174–2177.

[35] H. Tan, Z. Chen, Z. Xu, J. Sun, Z. Wang, R. Si, W. Zhuang, G. Guo, ACS Catal. 9 (2019) 3595–3603.

[36] R. Guo, Y. Qin, L. Qiao, J. Chen, X. Wu, Y. Yao, Catal. Commun. 88 (2017)

94–98.

[37] Y. Dong, Y. Shen, Y. Zhao, S. Wang, X. Ma, ChemCatChem 7 (2015) 2460–2466.

[38] H. Tan, Z. Wang, Z. Xu, J. Sun, Z. Chen, Q. Chen, Y. Chen, G. Guo, Catal. Sci. Technol. 7 (2017) 3785–3790.

[39] Y. Yamamoto, Catal. Surv. Asia 14 (2010) 103–110.

[40] Y. Yamamoto, T. Matsuzaki, S. Tanaka, K. Nishihira, K. Ohdan, A. Nakamura, Y. Okamoto, J. Chem. Soc. Faraday Trans. 93 (1997) 3721–3727.

[41] C. Wang, W. Xu, Z. Qin, H. Guo, X. Liu, S. Mintova, J. Energy Chem. 52 (2021) 191–201.

[42] Z. Qin, B. Shen, X. Gao, F. Lin, B. Wang, C. Xu, J. Catal. 278 (2011) 266–275.

[43] A.W. Burton, K. Ong, T. Rea, I.Y. Chan, Microporous Mesoporous Mater. 117 (2009) 75–90.

[44] G. Ye, Y. Sun, Z. Guo, K. Zhu, H. Liu, X. Zhou, M. Coppens, J. Catal. 360 (2018) 152–159.

[45] Z. Qin, K.A. Cychosz, G. Melinte, H. El Siblani, J. Gilson, M. Thommes, C. Fernandez, S. Mintova, O. Ersen, V. Valtchev, J. Am. Chem. Soc. 139 (2017) 17273–17276.

[46] H. Awala, J. Gilson, R. Retoux, P. Boullay, J. Goupil, V. Valtchev, S. Mintova, Nat. Mater. 14 (2015) 447–451.

[47] G. Engelhardt, U. Lohse, A. Samoson, M. Mägi, M. Tarmak, E. Lippmaa,

Zeolites 2 (1982) 59–62.

[48] J. Van Aelst, M. Haouas, E. Gobechiya, K. Houthoofd, A. Philippaerts, S.P. Sree, C.E.A. Kirschhock, P. Jacobs, J.A. Martens, B.F. Sels, F. Taulelle, J. Phys. Chem. C 118 (2014) 22573–22582.

[49] M. Valla, A.J. Rossini, M. Caillot, C. Chizallet, P. Raybaud, M. Digne, A. Chaumonnot, A. Lesage, L. Emsley, J.A. van Bokhoven, C. Copéret, J. Am. Chem. Soc. 137 (2015) 10710–10719.

[50] W. Lutz, C.H. Rüscher, D. Heidemann, Microporous Mesoporous Mater. 55 (2002) 193–202.

[51] J. Grand, S.N. Talapaneni, A. Vicente, C. Fernandez, E. Dib, H.A. Aleksandrov, G.N. Vayssilov, R. Retoux, P. Boullay, J. Gilson, V. Valtchev, S. Mintova, Nat. Mater. 16 (2017) 1010–1015.

[52] R. Kang, X. Wei, F. Bin, Z. Wang, Q. Hao, B. Dou, Appl. Catal. A 565 (2018) 46–58.

[53] U. Cimenler, B. Joseph, J.N. Kuhn, Appl. Catal. A 505 (2015) 494–500.

[54] M. Hartmann, A.G. Machoke, W. Schwieger, Chem. Soc. Rev. 45 (2016) 3313–3330.

[55] J. Zhou, Y. Wang, W. Zou, C. Wang, L. Li, Z. Liu, A. Zheng, D. Kong, W. Yang, Z. Xie, Ind. Eng. Chem. Res. 56 (2017) 9310–9321.

[56] Z. Mao, C.T. Campbell, ACS Catal. 9 (2019) 9465–9473.

[57] C. Wang, L. Han, P. Chen, G. Zhao, Y. Liu, Y. Lu, J. Catal. 337 (2016)

145–156.

[58] A.W. Petrov, D. Ferri, O. Kröcher, J.A. van Bokhoven, ACS Catal. 9 (2019) 2303–2312.

[59] G. Wang, S. Xu, L. Wang, Z. Liu, X. Dong, L. Wang, A. Zheng, X. Meng, F. Xiao, Chem. Commun. 54 (2018) 3274–3277.

[60] L. Karwacki, M.H.F. Kox, D.A. Matthijs De Winter, M.R. Drury, J.D. Meeldijk, E. Stavitski, W. Schmidt, M. Mertens, P. Cubillas, N. John, A. Chan, N. Kahn, S.R. Bare, M. Anderson, J. Kornatowski, B.M. Weckhuysen, Nat. Mater. 8 (2009) 959–965.

[61] A. Śrębowata, K. Tarach, V. Girman, K. Góra-Marek, Appl. Catal. B 181 (2016) 550–560.

[62] Y. Zheng, L. Kovarik, M.H. Engelhard, Y. Wang, Y. Wang, F. Gao, J. Szanyi, J. Phys. Chem. C 121 (2017) 15793–15803.

[63] P. Li, C. He, J. Cheng, C. Ma, B. Dou, Z. Hao, Appl. Catal. B 101 (2011) 570–579.

[64] C. Wang, Y. Jia, Z. Zhang, G. Zhao, Y. Liu, Y. Lu, Appl. Surf. Sci. 478 (2019) 840–845.

[65] A.F. Lee, J.N. Naughton, Z. Liu, K. Wilson, ACS Catal. 2 (2012) 2235–2241.

[66] S.P. Chenakin, G. Melaet, R. Szukiewicz, N. Kruse, J. Catal. 312 (2014) 1–11.

[67] C. Chen, J. Zhu, F. Chen, X. Meng, X. Zheng, X. Gao, F. Xiao, Appl. Catal. B 140–141 (2013) 199–205.

[68] Y. Lou, P. He, L. Zhao, H. Song, Fuel 183 (2016) 396–404.

[69] C. Wang, P. Chen, Y. Li, G. Zhao, Y. Liu, Y. Lu, J. Catal. 344 (2016) 173–183.

[70] K. Khivantsev, N.R. Jaegers, L. Kovarik, J.C. Hanson, F.F. Tao, Y. Tang, X. Zhang, I.Z. Koleva, H.A. Aleksandrov, G.N. Vayssilov, Y. Wang, F. Gao, J. Szanyi, Angew. Chem. Int. Ed. 57 (2018) 16672–16677.

[71] T. Frising, P. Leflaive, Microporous Mesoporous Mater. 114 (2008) 27–63.

[72] A.A. Rybakov, A.V. Larin, D.P. Vercauteren, Phys. Chem. Chem. Phys. 19 (2017) 20930–20940.

[73] Q. Zhang, X. Wu, Y. Li, R. Chai, G. Zhao, C. Wang, X. Gong, Y. Liu, Y. Lu, ACS Catal. 6 (2016) 6236–6245.

[74] R.J. Baxter, P. Hu, J. Chem. Phys. 116 (2002) 4379–4381.